Title

Emergence and Frustration of Magnetism with Variable-Range Interactions in a Quantum Simulator

Journal

Science, 340(6132)

ISSN

0036-8075

Authors

Islam, R
Senko, C
Campbell, WC
et al.

Publication Date

2013-05-03

DOI

10.1126/science.1232296

Peer reviewed

Emergence and Frustration of Magnetism with Variable-Range Interactions in a Quantum Simulator

R. Islam,[1]* C. Senko,[1] W. C. Campbell,[1]† S. Korenblit,[1] J. Smith,[1] A. Lee,[1] E. E. Edwards,[1] C.-C. J. Wang,[2]‡ J. K. Freericks,[2] C. Monroe[1]§

Frustration, or the competition between interacting components of a network, is often responsible for the emergent complexity of many-body systems. For instance, frustrated magnetism is a hallmark of poorly understood systems such as quantum spin liquids, spin glasses, and spin ices, whose ground states can be massively degenerate and carry high degrees of quantum entanglement. Here, we engineer frustrated antiferromagnetic interactions between spins stored in a crystal of up to 16 trapped $^{171}Yb^{+}$ atoms. We control the amount of frustration by continuously tuning the range of interaction and directly measure spin correlation functions and their coherent dynamics. This prototypical quantum simulation points the way toward a new probe of frustrated quantum magnetism and perhaps the design of new quantum materials.

Predicting the behavior of many-body quantum materials such as frustrated magnets is difficult because the number of relevant configurations scales exponentially with the number of particles (*1*–*3*). Feynman proposed the use of a quantum simulator for the task. Here, interactions are engineered in a "standard" quantum system to illuminate the physics behind the real material (*4*). Cold atoms are excellent standards for quantum simulations of magnetism, with the ability to tailor frustrated magnetic interactions and measure the individual atomic spins (*5*, *6*). Neutral atomic systems are typically limited to nearest-neighbor interactions (*7*), although geometrically frustrated interactions can be realized in certain optical lattice geometries (*8*). The strong Coulomb interaction between cold atomic ions (*9*) has led to the realization of long-range Ising couplings between individual trapped ion spins (*10*–*14*) and the observation of spin frustration and quantum entanglement in the smallest system of three spins (*15*).

Here, we report the implementation of variable-range antiferromagnetic (AFM) Ising interactions with up to 16 atomic ion spins, using optical dipole forces. We directly measure the emergence and frustration of magnetic ordering through spatially resolved imaging of the ions. The spins are initially polarized along a strong effective magnetic field transverse to the Ising couplings, and when the field is lowered, the spins order themselves according to the characterstics of the Ising interactions. We can increase the level of frustration by increasing the range of the interactions, which results in a more equitable balance of competing interactions and a suppression of magnetic order. The quantum coherence in the system is characterized by reversing the transverse field back to its initial value and comparing the resulting state with the initial state. These experiments present simulations in a nontrivial quantum system that approaches a complexity level at which it becomes difficult or impossible to calculate the spin dynamics.

Model

We simulate the quantum transverse Ising model with long-range AFM interactions in a one-dimensional spin chain, given by the Hamiltonian

$$H = \sum_{j<i} J_{ij}\sigma_x^{(i)}\sigma_x^{(j)} - B\sum_i \sigma_y^{(i)} \qquad (1)$$

where the Planck constant h is set to 1, $\sigma_\gamma^{(i)}(\gamma = x, y, z)$ are the spin-1/2 Pauli operators for the ith spin ($i = 1,2,\ldots N$), B is the effective transverse magnetic field, and $J_{ij} > 0$ is the Ising coupling between spins i and j, falling off with the lattice spacing $|i - j|$ approximately as

$$J_{ij} \approx \frac{J_0}{|i-j|^\alpha}, \qquad (2)$$

where $0 < \alpha < 3$ (*8*).

For $B >> J_{ij}$ on all pairs, the spins are polarized along the effective transverse magnetic field in the ground state $|\uparrow_y \uparrow_y \uparrow_y \ldots\rangle$ of the Hamiltonian in Eq. 1, where $|\uparrow_y\rangle$ denotes a spin along the $+y$ direction of the Bloch sphere. As the ratio of B to the Ising couplings is reduced, the system crosses over to an ordered state dictated by the form of the Ising couplings, and the spectrum of energy levels depends on the range of the interactions. For any finite $\alpha > 0$, we find by direct calculation that the staggered AFM states $|\uparrow\downarrow\uparrow\downarrow \ldots\rangle$ and $|\downarrow\uparrow\downarrow\uparrow \ldots\rangle$ constitute the doubly degenerate ground state manifold at $B = 0$, with the degeneracy arising from the time reversal or the global spin flip symmetry of the Hamiltonian. Here $|\uparrow\rangle$ and $|\downarrow\rangle$ are spin states oriented along the Ising or x direction of the Bloch sphere. Thus, the system exhibits nearest-neighbor AFM or Néel ordering at sufficiently low temperatures. When the interactions are uniform over all pairs of spins ($\alpha \to 0$), the system becomes maximally frustrated

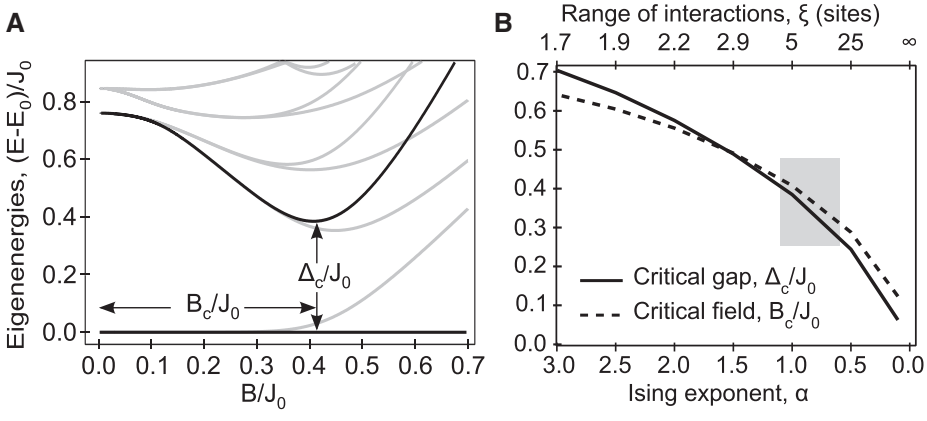

Fig. 1. Theoretical energy spectrum and critical gap in the long-range antiferromagnetic Ising model (Eq. 1) for $N = 10$ spins. (**A**) Low-lying energy states for $\alpha = 1$ (characteristic range of $\xi = 5$ sites) as a function of the dimensionless parameter B/J_0. The spacing between the ground state at $E = E_0$ and the first coupled excited state (black lines) reaches a bottleneck at a critical value B_c/J_0 with critical gap Δ_c. (**B**) Theoretical dependence of B_c/J_0 (dotted line) and Δ_c/J_0 (solid line) on the range of the interaction. As the interaction range increases, the competing long-range couplings make it easier to create excitations and the critical gap is reduced, so a relatively small effective transverse field can break the spin ordering. Both parameters approach zero as $\alpha \to 0$ or $\xi \to \infty$. Present experiments are performed with parameters in the shaded region.

[1]Joint Quantum Institute, University of Maryland Department of Physics and National Institute of Standards and Technology, College Park, MD 20742, USA. [2]Department of Physics, Georgetown University, Washington, DC 20057, USA.

*Present address: Department of Physics, Harvard University, Cambridge, MA 02138, USA.
†Present address: Department of Physics and Astronomy, University of California, Los Angeles, CA 90095, USA.
‡Present address: Theoretical Division, Los Alamos National Laboratory, Los Alamos, NM 87545, USA.
§Corresponding author. E-mail: monroe@umd.edu

and the excitation gap (Fig. 1A) closes, leading to a finite entropy density in the ground state. In this case, any spin configuration with a net magnetization of zero (1/2) for even (odd) numbers of spins belongs to the ground state.

Between the limits $B = 0$ and $B >> J_{ij}$, the energy spectrum features a minimum gap, whose position and size depends on the degree of frustration in the system, or the interaction range. (The interaction range is defined as the number of lattice spacings ξ where the interaction falls off to 20% of the nearest-neighbor Ising coupling: $\xi \equiv 5^{1/\alpha}$.) Figure 1A shows a few low-lying energy states of the Hamiltonian in Eq. 1 for an interaction range of $\xi = 5$ (corresponding to $\alpha = 1$). The first excited eigenstate merges with the ground state for small B/J_0 and has the same spin order as the ground state near $B/J_0 = 0$. The critical gap Δ_c between the ground and the first coupled excited state determines the adiabaticity criterion (*16*). Figure 1B compares the position (dotted line) and size (solid line) of the critical gap of the Hamiltonian for various ranges. As the range and hence the amount of frustration increases, the critical field is pushed toward zero, and the gap closes. To observe the effects of frustration, reflected in the density of states near the ground state, we quench the system by ramping the effective transverse magnetic field faster than the critical gap ($|\dot{B}/B| > \Delta_c$) to populate the lowest coupled excited states. The observed spin order depends on the resulting degree of excitation and hence on the level of frustration.

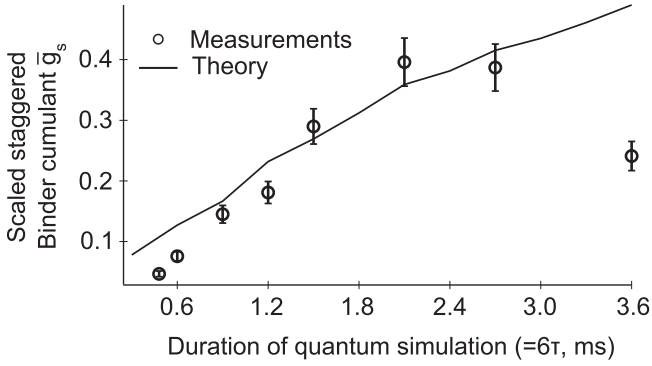

Fig. 2. Spin order versus speed of ramp, for $N = 10$ spins. The spins are initialized with $B/J_0 = 5$ and the transverse field is ramped exponentially down for six time constants, and the experiment is repeated for various values of time constant τ. Symbols (solid line) indicate the scaled staggered Binder cumulant $\bar{g}_s$, versus the total duration 6τ of the ramp measured (expected from theory). As the Hamiltonian evolves more slowly, the observed spin order shows more ground state order, and less excitation for ramp times under ~ 2.5 ms. For longer times, the spins become disordered, implying external decoherence in the system. Here (and in the following figures) the error bars include statistical fluctuations and estimated detection uncertainties.

Experiment

The spins are realized in a collection of $^{171}Yb^+$ ions confined in a linear radiofrequency (Paul) trap, with the effective spin-1/2 system represented by two hyperfine "clock" states within each ion $|\uparrow_z\rangle$ and $|\downarrow_z\rangle$, separated by the hyperfine frequency $\nu_{HF} = 12.642819$ GHz (*17*). The variable-range AFM Ising interactions are generated by applying off-resonant spin-dependent optical dipole forces (*11*) that drive stimulated Raman transitions between the spin states while modulating the Coulomb interaction between the ions in a controlled way (*18*). The effective magnetic field is generated by simultaneously driving coherent transitions between the spin states with a $\pi/2$-phase shift with respect to the dipole force beams. At any time, we measure the state of the spins by illuminating the ions with resonant radiation and collecting state-dependent fluorescence on an imager with site-resolving optics (*17*). From this information, we can extract all spin correlation functions (*18*).

The quantum simulation begins by optically pumping all spins to the $|\downarrow_z\rangle$ state and then coherently rotating them all about the x axis of the Bloch sphere to initialize each spin in state $|\uparrow_y\rangle$ along the effective transverse magnetic field.

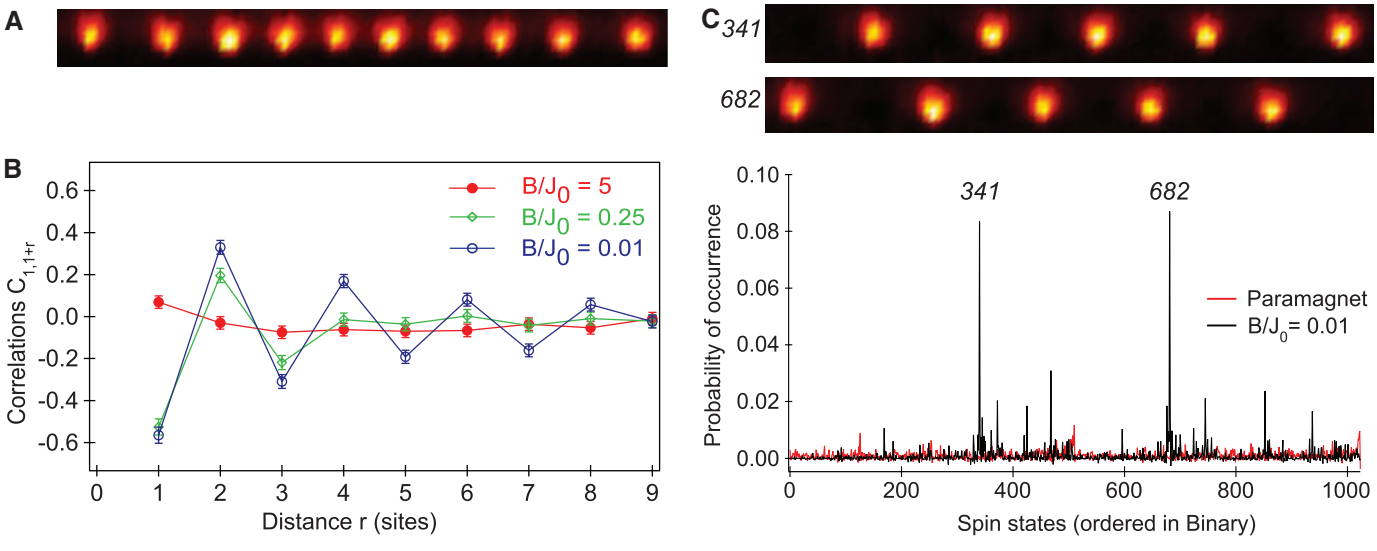

Fig. 3. Quantum phase transition from a paramagnet to an antiferromagnet (Eq. 1), with $J_{ij} \approx |i - j|^{-1.05}$ in a system of 10 spins. The exponent ($\alpha = 1.05$) is estimated from the average couplings between spins in this inhomogeneous system. (**A**) Image of 10 trapped ions, with a distance of 22 μm between the first and last ion. (**B**) Measured two-point correlation function between a chosen spin (on the edge) and the other spins separated by r lattice sites, $C_{1,1+r} = \langle \sigma_x^{(1)} \sigma_x^{(1+r)} \rangle - \langle \sigma_x^{(1)} \sigma_x^{(1+r)} \rangle$, averaged over 4000 experiments for each value of the parameter B/J_0. For $B/J_0 = 5$, the spins are initially polarized along the transverse y field with little correlation along the Ising x direction. As the field is reduced, the spins cross over to predominantly AFM states $|\uparrow\downarrow\uparrow\downarrow\ldots\rangle$ and $|\downarrow\uparrow\downarrow\uparrow\ldots\rangle$, resulting in alternating signs in the two-point correlations with separation. The solid lines are shown to guide the eye. (**C**) Measured occurrence probability of all $2^{10} = 1024$ states at $B/J_0 \approx 5$ (paramagnetic state, red trace) and $B/J_0 \approx 0.01$ (AFM phase, black trace). The states are listed in binary order, with spin $|\downarrow\rangle \equiv 0$ and $|\uparrow\rangle \equiv 1$. The residual peaks in the red trace are consistent with detection errors biased toward states with many $|\uparrow\rangle$ spins such as 127, 511, and 1023. The two tall peaks in the black trace at 341 (0101010101) and 682 (1010101010) correspond to two Néel-ordered staggered AFM states, shown with camera images of these cases and contributing ~17% to the population.

The Hamiltonian (Eq. 1) is then switched on with an initial field $B_0 \approx 5\ J_0$, where J_0 (~1 kHz) is the average nearest-neighbor Ising coupling, thus preparing the spins in the ground state of the initial Hamiltonian with a fidelity better than 97%. The effective magnetic field is ramped down exponentially in time with a time constant of 400 μs to a final value B of the transverse field, but no longer than 2.4 ms overall, to avoid decoherence effects present in the system (see Fig. 2). At this point, the Hamiltonian is switched off, freezing the spins for measurement. We then measure the x or y component of each spin $\sigma_x^{(i)}$ or $\sigma_y^{(i)}$ by first rotating our measurement axes with an appropriate global π/2 pulse similar to the initialization procedure, before capturing the spin-dependent fluorescence on the imager. The experiments are repeated 2000 to 4000 times to measure expectation values of certain spin operators and correlation functions (denoted by ⟨... ⟩).

Order Parameters and Correlation Functions

From these measurements, we can construct order parameters appropriate for observing low-energy AFM states. Various moments of the staggered magnetization operator $m_s = \frac{1}{N}\sum_{i=1}^{N}(-1)^i\sigma_x^{(i)}$ distinguish between paramagnetic and AFM order, and also quantify spin flip excitations. In particular, the normalized fourth moment of this magnetization, known as the Binder cumulant (*19*) $g_s = \langle(m_s - \langle m_s\rangle)^4\rangle/\langle(m_s - \langle m_s\rangle)^2\rangle^2$, scaled to $\overline{g}_s = (g_s^0 - g_s)/(g_s^0 - 1)$ to remove finite size effects, varies from $\overline{g}_s = 0$ to $\overline{g}_s = 1$ as the paramagnetic state gives way to AFM order (see Fig. 2). Here $g_s^0 = 3 - 2/N$ is the Binder cumulant in a perfect paramagnetic state of the N spins. We can also form any correlation function of the spins such as the two-point correlation $C_{i,j} = \langle\sigma_x^{(i)}\sigma_x^{(j)}\rangle - \langle\sigma_x^{(i)}\rangle\langle\sigma_x^{(j)}\rangle$, allowing a direct probe of spin order for each experimental realization. The Fourier transform of this correlation function is the structure function $S(k) = \frac{1}{N-1}\left|\sum_{r=1}^{N-1}C(r)e^{ikr}\right|$, where $C(r) = \frac{1}{N-r}\sum_{m=1}^{N-r}C_{m,m+r}$ is the average correlation over r sites in the chain. The structure function shows spin order versus wave number k, with $S(k = \pi)$ singling out the presence of the nearest-neighbor Néel AFM order.

Figure 3 shows the onset of AFM ordering in the quantum simulation of the frustrated transverse field Ising model in a system of 10 spins. Two-point spin correlations $C_{1,r}$ between a chosen edge spin and the other spins are presented in Fig. 3B at various stages in the ramp $B/J_0 = 5$, 0.25, and 0.01. For larger transverse magnetic fields, there are no appreciable correlations between the spin components along the Ising direction. As the ratio of B/J_0 is lowered, however, a zig-zag pattern emerges, with negative (positive) correlations between spins separated by odd (even) lattice spacings. For $B/J_0 \approx 0.01$, the nearest-neighbor spin correlation reaches about 60%, and the correlation length (defined to be the distance at which the absolute correlation drops to $1/e$ of the nearest neighbor value) reaches about six lattice sites. The effective field was ramped exponentially down from $B/J_0 \approx 5$ with a time constant of 400 μs in this experiment. This ramping is not slow enough to be adiabatic, and the diabatic effects prevent the spin ordering from reaching a perfect AFM phase. Figure 3C shows the measured probabilities of all $2^{10} = 1024$ possible spin states measured along the Ising x direction, sorted in binary order with spin $|\downarrow\rangle \equiv 0$ and $|\uparrow\rangle \equiv 1$. The net detection fidelity of each spin is ~97%, after postfiltering the measurements based on calibrating the known detection errors for each spin (*18*, *20*). The initial paramagnetic phase shown in red ($B/J_0 \approx 5$) exhibits a roughly uniform probability of 1/1024 ≈ 0.1% for each state (the residual peaks in the red trace are consistent with detection errors). The spin-ordered phase shown in black ($B/J_0 = 0.01$) displays the emergence of the two AFM states, each with an occupation probability of about 8.5%. Other prominent peaks correspond to single spin-flips and other low-lying excitations from the two ground states.

In Fig. 4, we probe the frustration in the system for various ranges of interactions. Here, we look at the spin order achieved in the quantum simulation when the external magnetic field is ramped down to $B/J_0 \approx 0.01$ for four different ranges of interactions. In Fig. 4A, we show the measured structure function $S(k)$ at wave vector values $k = \frac{\pi}{10}, \frac{2\pi}{10}, \ldots, \pi$ from the measured two-point correlation functions. To directly compare the different interaction ranges, we choose the same external magnetic field ramp time constant, $\tau = 0.4/J_0$. As the range of interaction increases, the ground state AFM order (given by the structure function peak at $k = \pi$) disappears, reflecting increased occupation of the excited states as the frustration grows. Figure 4B displays the observed distribution of energy $P(E_i)$ for $\alpha = 1.05$ (shorter range) and $\alpha = 0.76$ (longer range) power-law exponents, along with the cumulative energy distribution function. The eigenenergies of each configuration are calculated using Eq. 1 with $B = 0$. For the longer-range interactions, excitations are more prevalent, and the energy gap between the ground and the first excited state is reduced, both of which are signatures of increasing frustration in the system. The observed final entropy per particle $S = -\frac{1}{N}\sum_i P(E_i)\log P(E_i)$ is seen to increase from 0.832 to 0.903 as the interaction range grows from $\alpha = 1.05$ ($\xi = 4.6$ sites) to $\alpha = 0.67$ ($\xi = 11$ sites), which is also a signature of the increased frustration in the system. As a reference, the paramagnetic state distribution shows an entropy per particle of 0.959, which is slightly less than unity because of detection errors.

Quantum Coherence

The above measurements of the state distribution concern only the diagonal components or

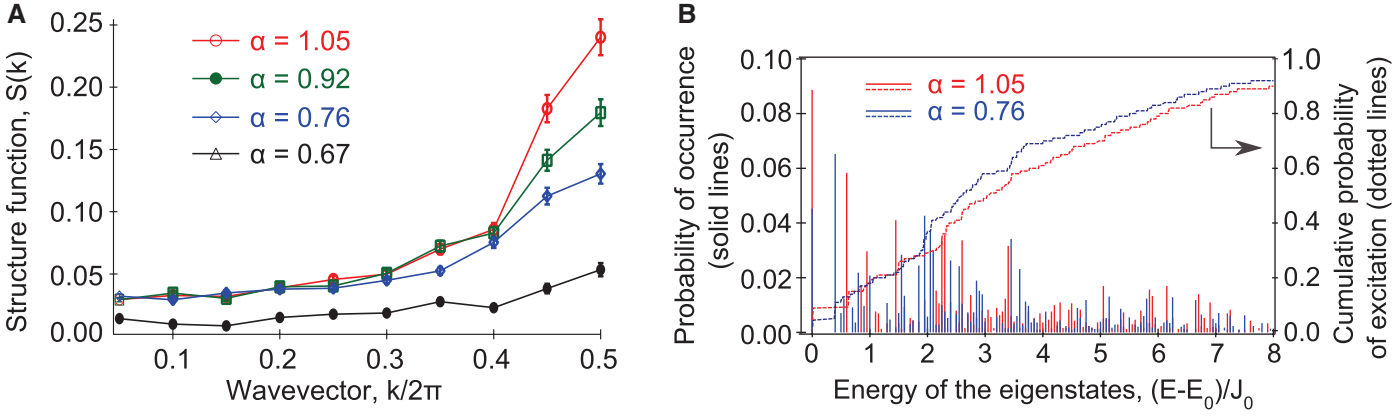

Fig. 4. (A) Structure function *S*(*k*) versus wave vector *k* for various ranges of AFM interactions, for $B/J_0 = 0.01$ in a system of $N = 10$ spins. The increased level of frustration for the longer-range interactions reduces the observed antiferromagnetic spin order. The detection errors may be larger than shown here for the longest range of interactions, owing to spatial crosstalk from their closer spacing. (**B**) Distribution of observed states in the spin system, sorted according to their energy E_i that was previously calculated by diagonalizing Eq. 1 with $B = 0$. Data are presented for two ranges (red for $\alpha = 1.05$ and blue for $\alpha = 0.76$). The dashed lines indicate the cumulative energy distribution functions for these two ranges.

populations of the density matrix. To characterize the quantum coherence in the simulation, we retrace the external magnetic field back to its initial value after ramping it down to almost zero and measure each spin along the transverse (y) magnetic field. Figure 5 shows the distribution of the measured value m_y of the total transverse spin operator $S_y = \Sigma_i \sigma_y^{(i)}$ at three different times: first at the beginning of the simulation, second when the transverse field has been ramped down to nearly zero, and third after the transverse field returns to its initial value ($\alpha = 0.92$ for these data). The initial state is ideally a delta function at $\langle S_y \rangle = 10$, but finite detection efficiency broadens the distribution. At the lowest value of the field ($B/J_0 \approx 0.01$), the transverse magnetization is distributed near $\langle S_y \rangle = 0$, as the spins are presumably ordered along the Ising x direction. When the external field is ramped back to its initial state, the distribution of the total spin returns toward the initial distribution, with an average magnetization that is approximately $\langle S_y \rangle = 68(4)\%$ of its initial value, indicating that some level of quantum coherence is maintained throughout the simulation. This number is in agreement with the theoretically estimated average magnetization of $\langle S_y \rangle \approx 70\%$ of its initial value, obtained by numerically integrating the Schrödinger's equation without any decoherence.

To probe decoherence in the simulation, we repeat the experiment with various ramping speeds of the effective magnetic field. In Fig. 2, we plot the AFM order parameter g_s versus the total duration for the experiment for a long-range coupling ($\alpha = 1.05$) for $N = 10$ spins. Each data point represents the spin order achieved after ramping the magnetic field B down exponentially from $5J_0$ for a total duration of six time constants. The AFM order grows with slower ramping, as expected, for up to $\tau = 400$ μs. But we also observe a saturation and then decay in the spin order, which might indicate the presence of decoherence in the system at long times. During the simulation, spontaneous Raman scattering from the optical beams is expected to occur at a rate of less than 6 s^{-1} per spin (*21*), which is consistent with separate measurements of the spin relaxation from a single spin and is therefore not expected to contribute to decoherence given the time scales in the experiment. The phonon population is expected to be well under 10% for all the data presented here (*22*). A principal source of decoherence appears to be the intensity fluctuations in the Raman beams, from beam pointing instabilities and fluctuations in the optical power.

Maintaining adiabaticity while ramping the magnetic field down is more difficult when the Ising interactions in the experiment are frustrated, because the relevant energy gaps are smaller. To directly compare frustrated versus nonfrustrated systems, we execute quantum simulations of both long-range AFM and ferromagnetic (FM) Ising models in a system of $N = 16$ spins (Fig. 6). For the FM experiment (Fig. 6C), we initialize the spins in the highest-energy state with respect to the transverse field $|\downarrow_y \downarrow_y \downarrow_y \ldots\rangle$ and ramp the field down as before (*10*, *15*). For the AFM experiment with the same ramp rate, we find that the best AFM nearest-neighbor correlation (Fig. 6A) is only 30(3)%, corresponding to a staggered magnetization of about 30(2)%, whereas the simulation of the FM model shows a clear FM spin order across the chain (Fig. 6B), reaching 73(3)% magnetization. We have also observed a level of 70(10)% FM magnetization emerging in $N = 18$ spins (*18*).

The interacting spin system that we study is approaching a complexity level at which it becomes difficult or impossible to predict its behavior. Static properties such as the ground state order or the excited state energies can be calculated for hundreds of spins using Monte Carlo methods (*23*); however, the calculation of dynamics of fully connected spin models is currently limited to approximately $N = 30$ spins (*24*, *25*).

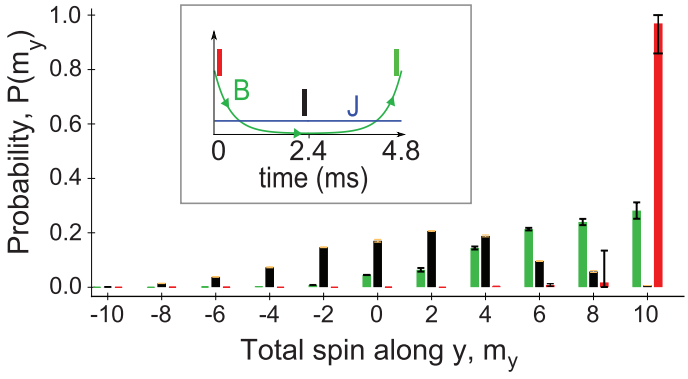

Fig. 5. Quantum coherence in the simulation, in a system of $N = 10$ spins. Probabilities of different values of the total spin component along y in the initial polarized state (red), when the transverse field is ramped to ≈0.01 J_0 (black), and when the transverse field is reversed back to its initial value (green). After reversal, the y magnetization returns to ~68(4)% of its initial value, indicating quantum coherence in the evolution. The trajectory of the transverse field (B, in green) and all the Ising couplings (J, in blue) are shown in the inset. $\alpha = 0.92$ for these data.

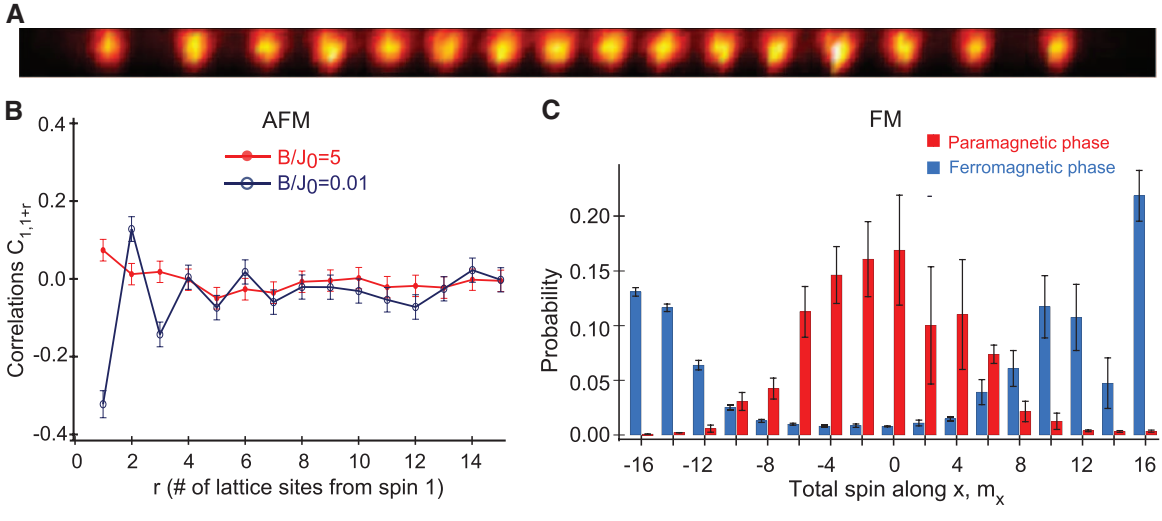

Fig. 6. Magnetic ordering in N=16 spins. (**A**) Image of 16 trapped ions, with a distance of 30 μm between the first and last ion. (**B**) Pair correlation function measured at various stages of the quantum simulation, for $B/J_0 = 5$ (red) and $B/J_0 = 0.01$ (blue) in an AFM coupling falling off with distance as $J_{ij} \sim |i - j|^{-1}$ among $N = 16$ spins. Small amounts of staggered order are seen, tempered by the small gaps and frustration in the low-energy states. (**C**) In contrast, for all FM couplings (again with $J_{ij} \sim |i - j|^{-1}$), the gaps are large and clear FM order is seen. Here the measured distribution of magnetization is plotted. The paramagnetic phase of 16 spins is indicated in red, and after the field is ramped to nearly zero, the distribution clearly bifurcates, indicating population weighted heavily toward the FM states $|\downarrow\downarrow\downarrow\ldots\rangle$ and $|\uparrow\uparrow\uparrow\ldots\rangle$, indicated in blue. The resulting magnitude magnetization is ~73%.

Small ion trap quantum simulators such as that reported here may soon reach this milestone with technical upgrades in the hardware, including lower vacuum chamber pressures to prevent collisions with the background gas, better stability of the optical intensities, and higher optical power so that fluctuations in the beam inhomogeneities can be suppressed.

References and Notes

1. H. T. Diep, *Frustrated Spin Systems* (World Scientific, Singapore, 2005).
2. R. Moessner, A. P. Ramirez, *Phys. Today* **59**, 24 (2006).
3. S. Sachdev, *Quantum Phase Transitions* (Cambridge Univ. Press, Cambridge, 1999).
4. R. Feynman, *Int. J. Theor. Phys.* **21**, 467 (1982).
5. I. Bloch, J. Dalibard, S. Nascimbéne, *Nat. Phys.* **8**, 267 (2012).
6. R. Blatt, C. F. Roos, *Nat. Phys.* **8**, 277 (2012).
7. J. Simon *et al.*, *Nature* **472**, 307 (2011).
8. G.-B. Jo *et al.*, *Phys. Rev. Lett.* **108**, 045305 (2012).
9. D. Porras, J. I. Cirac, *Phys. Rev. Lett.* **92**, 207901 (2004).
10. A. Friedenauer, H. Schmitz, J. T. Glueckert, D. Porras, T. Schaetz, *Nat. Phys.* **4**, 757 (2008).
11. K. Kim *et al.*, *Phys. Rev. Lett.* **103**, 120502 (2009).
12. R. Islam *et al.*, *Nat. Commun.* **2**, 377 (2011).
13. J. W. Britton *et al.*, *Nature* **484**, 489 (2012).
14. A. Khromova *et al.*, *Phys. Rev. Lett.* **108**, 220502 (2012).
15. K. Kim *et al.*, *Nature* **465**, 590 (2010).
16. E. E. Edwards *et al.*, *Phys. Rev. B* **82**, 060412 (2010).
17. S. Olmschenk *et al.*, *Phys. Rev. A* **76**, 052314 (2007).
18. See supplementary materials on *Science* Online.
19. K. Binder, *Phys. Rev. Lett.* **47**, 693 (1981).
20. C. Shen, L.-M. Duan, *New J. Phys.* **14**, 053053 (2012).
21. W. C. Campbell *et al.*, *Phys. Rev. Lett.* **105**, 090502 (2010).
22. C.-C. J. Wang, J. K. Freericks, *Phys. Rev. A* **86**, 032329 (2012).
23. R. Moessner, S. L. Sondhi, *Phys. Rev. B* **63**, 224401 (2001).
24. A. W. Sandvik, *Phys. Rev. Lett.* **104**, 137204 (2010).
25. Quantum Monte Carlo algorithms can be used to calculate static equilibrium properties of the transverse field Ising model for large numbers of interacting spins, so ground states and static correlation functions can indeed be calculated for large systems (*23*). However, the calculation of dynamics and nonequilibrium behavior of quantum spin models is not currently feasible for these Monte Carlo approaches, and in the presence of frustrated long-range interactions, the general behavior of such systems requires exact diagonalization. Other techniques such as the density matrix renormalization group become too difficult with long-range interactions. Because the size of the Hilbert space grows exponentially with the number of spins, sparse-matrix techniques such as the Lanczos method must therefore be used. Current state-of-the-art work on such systems is limited to sizes on the order of 30 to 35 spins (*24*).

Acknowledgments: We thank E. Demler, L. Duan, D. Huse, K. Kim, P. Richerme, R. Sensarma, and P. Zoller for critical discussions. This work is supported by the U.S. Army Research Office (ARO) award W911NF0710576 with funds from the Defense Advanced Research Projects Agency Optical Lattice Emulator Program, ARO award W911NF0410234 with funds from the Intelligence Advanced Research Projects Activity, and the NSF Physics Frontier Center at the Joint Quantum Institute. J.K.F. was also supported by the McDevitt bequest at Georgetown.

Supplementary Materials

www.sciencemag.org/cgi/content/full/340/6132/583/DC1
Supplementary Text
Fig. S1
References (*26*–*28*)

2 November 2012; accepted 8 February 2013
10.1126/science.1232296

Kepler-62: A Five-Planet System with Planets of 1.4 and 1.6 Earth Radii in the Habitable Zone

William J. Borucki,[1]* Eric Agol,[2] Francois Fressin,[3] Lisa Kaltenegger,[3,4] Jason Rowe,[5] Howard Isaacson,[6] Debra Fischer,[7] Natalie Batalha,[1] Jack J. Lissauer,[1] Geoffrey W. Marcy,[6] Daniel Fabrycky,[8,9] Jean-Michel Désert,[3] Stephen T. Bryson,[1] Thomas Barclay,[10] Fabienne Bastien,[11] Alan Boss,[12] Erik Brugamyer,[13] Lars A. Buchhave,[14,15] Chris Burke,[5] Douglas A. Caldwell,[5] Josh Carter,[3] David Charbonneau,[3] Justin R. Crepp,[16,17] Jørgen Christensen-Dalsgaard,[18] Jessie L. Christiansen,[5] David Ciardi,[19] William D. Cochran,[13] Edna DeVore,[5] Laurance Doyle,[5] Andrea K. Dupree,[3] Michael Endl,[13] Mark E. Everett,[20] Eric B. Ford,[21] Jonathan Fortney,[8] Thomas N. Gautier III,[22] John C. Geary,[3] Alan Gould,[23] Michael Haas,[1] Christopher Henze,[1] Andrew W. Howard,[24] Steve B. Howell,[1] Daniel Huber,[1] Jon M. Jenkins,[5] Hans Kjeldsen,[18] Rea Kolbl,[6] Jeffery Kolodziejczak,[25] David W. Latham,[3] Brian L. Lee,[2] Eric Lopez,[8] Fergal Mullally,[5] Jerome A. Orosz,[26] Andrej Prsa,[27] Elisa V. Quintana,[5] Roberto Sanchis-Ojeda,[30] Dimitar Sasselov,[3] Shawn Seader,[5] Avi Shporer,[8,28] Jason H. Steffen,[29] Martin Still,[10] Peter Tenenbaum,[5] Susan E. Thompson,[5] Guillermo Torres,[3] Joseph D. Twicken,[5] William F. Welsh,[26] Joshua N. Winn[30]

We present the detection of five planets—Kepler-62b, c, d, e, and f—of size 1.31, 0.54, 1.95, 1.61 and 1.41 Earth radii ($R_\oplus$), orbiting a K2V star at periods of 5.7, 12.4, 18.2, 122.4, and 267.3 days, respectively. The outermost planets, Kepler-62e and -62f, are super–Earth-size (1.25 $R_\oplus$ < planet radius ≤ 2.0 $R_\oplus$) planets in the habitable zone of their host star, respectively receiving 1.2 ± 0.2 times and 0.41 ± 0.05 times the solar flux at Earth's orbit. Theoretical models of Kepler-62e and -62f for a stellar age of ~7 billion years suggest that both planets could be solid, either with a rocky composition or composed of mostly solid water in their bulk.

Kepler is a NASA Discovery-class mission designed to determine the frequency of Earth-radius planets in and near the habitable zone (HZ) of solar-like stars (*1*–*6*). Planets are detected as "transits" that cause the host star to appear periodically fainter when the planets pass in front of it along the observer's line of sight. Kepler-62 [Kepler Input Catalog (KIC) 9002278, Kepler Object of Interest (KOI) 701] is one of about 170,000 stars observed by the Kepler spacecraft. On the basis of an analysis of long-cadence photometric observations from Kepler taken in quarters 1 through 12 (13 May 2009 through 28 March 2012), we report the detection of five planets orbiting Kepler-62, including two super–Earth-size planets in the HZ as well as a hot Mars-size planet (Fig. 1 and Table 1). Before validation, three of these objects were designated as planetary candidates KOI-701.01, 701.02, and 701.03 in the Kepler 2011 catalog (*7*) and the Kepler 2012 catalog (*8*). KOI-701.04 and 701.05 were subsequently identified using a larger data sample (*9*).

Analysis of high-resolution spectra indicates that Kepler-62 is a K2V spectral type with an estimated mass and radius (in solar units) of 0.69 ± 0.02 $M_\odot$ and 0.63 ± 0.02 $R_\odot$ (*9*). Examination of the sky close to Kepler-62 showed the presence of only one additional star that contributed as much as 1% to the total flux (figs. S3 and S4) (*9*). Warm-Spitzer observations (fig. S9) and the analysis of centroid motion (table S1) were consistent with the target star as the source of the transit signals (Fig. 1 and fig. S1). We computed the radius, semimajor axis, and radiative equilibrium temperature of each planet (Table 1) on the basis of light curve modeling given the derived stellar parameters (table S3).

The masses of the planets could not be directly determined using radial velocity (RV) measurements of the host star because of the planets' low masses, the faintness and variability of the star, and the level of instrument noise. In the absence of a detected signal in the RV measurements (*9*), we statistically validated the planetary nature of Kepler-62b through -62f with the BLENDER procedure (*10*–*13*) by comparing the probability of eclipsing binaries and other false-positive scenarios to bona fide transiting planet signals (*14*–*18*).

To systematically explore the different types of false positives that can mimic the signals, we generated large numbers of synthetic light curves that blend together light from multiple stars and planets over a wide range of parameters, and then compared each blend with the Kepler photometry (Fig. 2). We rejected blends that resulted in light curves inconsistent with the observations.

www.sciencemag.org/cgi/content/full/340/6132/583/DC1

Supplementary Materials for

Emergence and Frustration of Magnetism with Variable-Range Interactions in a Quantum Simulator

R. Islam, C. Senko, W. C. Campbell, S. Korenblit, J. Smith, A. Lee, E. E. Edwards, C.-C. J. Wang, J. K. Freericks, C. Monroe*

*Corresponding author. E-mail: monroe@umd.edu

Published 3 May 2013, *Science* **340**, 583 (2013)
DOI: 10.1126/science.1232296

This PDF file includes:

Supplementary Materials

Generating variable-range AFM Ising interactions The Ising interaction is generated by globally addressing the ions with two off-resonant laser beams at $\lambda = 355$ nm (*21*), intersecting at right angles with wavevector difference $\Delta k = 2\pi\sqrt{2}/\lambda$ along a principal axis of transverse ion motion (*26*). These beams have beatnote frequencies $\nu_{HF} \pm \mu$ which drive stimulated Raman transitions near the upper and lower motional sidebands of transverse motion in order to impart a spin-dependent optical dipole force (*27*). By setting the beatnotes sufficiently far from the sidebands, motional excitations can be made negligible, resulting in a nearly pure spin-spin coupling mediated by the Coulomb interaction (*11*). The effective transverse magnetic field is generated by simultaneously driving a resonant stimulated Raman transition between the spin states with a beatnote frequency ν_{HF} and a phase that is shifted by $\pi/2$ with respect to the mean phase of the sideband fields. The resulting Ising coupling matrix J_{ij} is given by a sum over contributions from each normal mode of collective motion at frequency ν_m,

$$J_{ij} = \Omega^2 \nu_R \sum_{m=1}^{N} \frac{b_{i,m} b_{j,m}}{\mu^2 - \nu_m^2} \tag{S1}$$

where $\nu_R = h/M\lambda^2 = 18.5$ kHz is the recoil frequency associated with the dipole force on a single $^{171}\mathrm{Yb}^+$ion of mass M, $b_{i,m}$ is the orthonormal component of ion i with mode m, and Ω is the (uniform) single spin flip Rabi frequency, proportional to the laser intensity at each ion. The symmetric detuning μ of the beatnote from the spin-flip transition controls the sign and range of the interactions (*11*). When μ is set larger than the highest (center-of-mass or COM) mode frequency ν_1, every interaction is AFM, and we can empirically approximate Eq. S1 as falling off with distance as a power law $J_{ij} \approx J_0/|i-j|^\alpha$ with $0 < \alpha < 3$ (*9*) and $J_0 \propto 1/N$. While the COM mode mediates a uniform interaction between all pairs of spins, the other modes introduce non-uniformity in the interactions, and effectively reduce the range of AFM interaction. In practice, we control the interaction range by changing the bandwidth of the transverse mode spectrum, achieved by varying the axial confinement of the ions in the Paul trap. The Ising couplings J_{ij} depend not only on the spatial separation $|i-j|$, but also on the

site i itself due to the finite size of the system, with $\sim 10\%$ inhomogeneities across the chain. We average over all the couplings between spins separated by a given number of lattice sites to estimate the power law range exponent α in Eq. 2 (*13*).

In the experiment we use global Raman beams each with an optical power of approximately 1W, having horizontal and vertical waists of about 150 μm and 7 μm respectively, to address the ions. This produces a spin-flip Rabi frequency $\Omega \approx 600$ kHz on resonance, with less than 5% inhomogeneity across the chain. We set the beatnote detuning to $\mu \approx \nu_1 + 3\eta\Omega$, where $\eta = \sqrt{\nu_R/\nu_1}$ is the single ion Lamb-Dicke parameter. This keeps the (primarily COM) phonon excitation probabilities sufficiently low for any setting of the range. The typical nearest neighbor Ising coupling is $J_0 \sim 1$ kHz for $N = 10$ spins. In principle, the Ising interaction range can be varied from uniform to dipolar ($0 < \alpha < 3$), but in this experiment the axial frequency was only varied between 0.62 MHz and 0.95 MHz, and given the COM transverse frequency of $\nu_1 = 4.8$ MHz, this results in a range of Ising power-law exponents $0.7 < \alpha < 1.2$, or a variation of the range of interactions between $\xi = 4$ to $\xi = 10$ sites.

Accounting for finite detection efficiency of N-particle correlations We detect the spin states using spin-dependent fluorescence collected through f/2.1 optics onto an intensified charge-coupled-device (ICCD) camera or a photomultiplier tube (PMT). The spin state $|\uparrow_z\rangle$ fluoresces from the near-resonant detection beam and appears bright, while the spin state $|\downarrow_z\rangle$ scatters little from the off-resonant detection beam and appears dark. The imager has single-site resolution, allowing us to directly measure the two point correlations to probe the AFM order. The spin detection efficiency is the symmetric probability of correctly diagnosing a particular spin state from measurement, and is typically limited by the residual overlaps in the bright and dark flourescence count distribution (*28*).

The detection efficiency for a single spin is observed to be $\epsilon \approx 95\%$ on the ICCD imager, which is lower than the 98% efficiency on the PMT, due to additional electronic and readout noise. For a crystal of $N = 10$ ions, the spatial overlap between the ion images degrades the

detection efficiency even further. To account for this spatial crosstalk, we fit each single shot image in the experiment to a sum of N Gaussians, where N is the number of ions. The center and width of the Gaussians are pre-calibrated from images of all spins prepared in their bright states, with background subtraction from all spins prepared in their dark states. This results in a spread of detection efficiencies between $93 - 97\%$ per spin, depending upon the state of the neighboring spins. The probability of correctly identifying a $N = 10$-body spin state is thus in the range of $\epsilon^N \sim 50 - 75\%$, so we post-process the detected states to improve this value, following the ideas in Ref. (*20*). The probability of incorrectly assigning an N-qubit state $|i\rangle$ to the actual underlying state $|j\rangle$ is $M_{ij} = (1-\epsilon)^{\beta_{ij}}\epsilon^{N-\beta_{ij}}$, where β_{ij} is the number of positions that the N-qubit state $|j\rangle$ differs from $|i\rangle$ through bit flips. The observed probability distribution of all 2^N states is then given by $P'_i = \sum_j M_{ij}P_j$, where P_j is the underlying actual distribution of states, which can be obtained by simply inverting the experimentally measured matrix M_{ij} and forming $P_i = \sum_j M^{-1}_{ij}P'_j$. This increases the effective detection fidelity per spin to roughly 97%, similar to that of a single ion with a PMT. Detection errors are included in all the error bars presented, and represent the range of measurements expected from a representative range of detection efficiencies. Some entries of the post-processed probabilities are slightly negative, due to fluctuations in absolute fluorescence levels that impact the values in the matrix M_{ij} during measurement.

N=18 spin ferromagnetic simulation

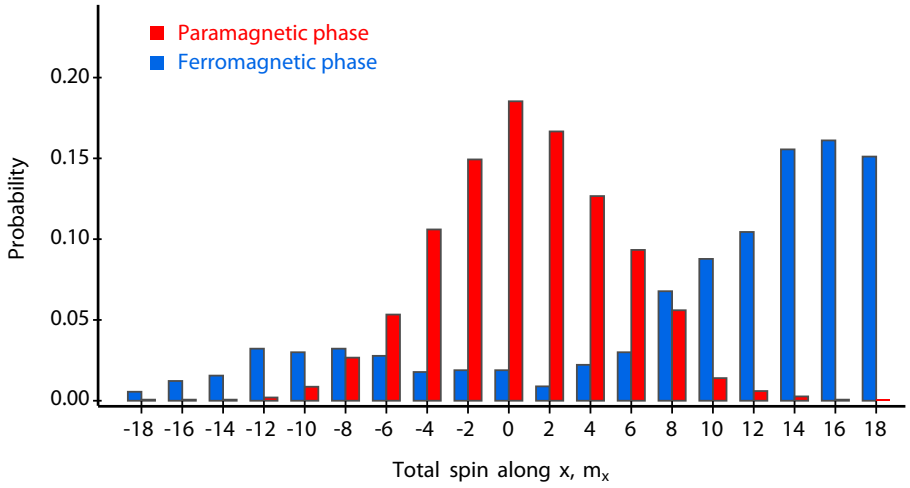

Figure S1: Distribution of magnetization in a collection of $N = 18$ spins under the influence of ferromagnetic Ising couplings that fall off as $J_{ij} \sim |i - j|^{-1}$. The paramagnetic phase of the spins is indicated in red, and after the field is ramped to nearly zero, the distribution splits into population weighted heavily towards the FM states $|\downarrow\downarrow\downarrow \cdots\rangle$ and $|\uparrow\uparrow\uparrow \cdots\rangle$, indicated in blue. The resulting magnitude magnetization is approximately $70(10)\%$. The clear bias toward the state $|\uparrow\uparrow\uparrow \cdots\rangle$ may be due to a background effective field along the Ising (axial) direction.

References and Notes

1. H. T. Diep, *Frustrated Spin Systems* (World Scientific, Singapore, 2005).

2. R. Moessner, A. P. Ramirez, Geometrical frustration. *Phys. Today* **59**, 24 (2006). doi:10.1063/1.2186278

3. S. Sachdev, *Quantum Phase Transitions* (Cambridge Univ. Press, Cambridge, UK, 1999).

4. R. Feynman, Simulating physics with computers. *Int. J. Theor. Phys.* **21**, 467 (1982). doi:10.1007/BF02650179

5. I. Bloch, J. Dalibard, S. Nascimbéne, Quantum simulations with ultracold quantum gases. *Nat. Phys.* **8**, 267 (2012). doi:10.1038/nphys2259

6. R. Blatt, C. F. Roos, Quantum simulations with trapped ions. *Nat. Phys.* **8**, 277 (2012). doi:10.1038/nphys2252

7. J. Simon *et al*., Quantum simulation of antiferromagnetic spin chains in an optical lattice. *Nature* **472**, 307 (2011). doi:10.1038/nature09994 Medline

8. G.-B. Jo *et al*., Ultracold atoms in a tunable optical kagome lattice. *Phys. Rev. Lett.* **108**, 045305 (2012). doi:10.1103/PhysRevLett.108.045305 Medline

9. D. Porras, J. I. Cirac, Effective quantum spin systems with trapped ions. *Phys. Rev. Lett.* **92**, 207901 (2004). doi:10.1103/PhysRevLett.92.207901 Medline

10. A. Friedenauer, H. Schmitz, J. T. Glueckert, D. Porras, T. Schaetz, Simulating a quantum magnet with trapped ions. *Nat. Phys.* **4**, 757 (2008). doi:10.1038/nphys1032

11. K. Kim *et al*., Entanglement and tunable spin-spin couplings between trapped ions using multiple transverse modes. *Phys. Rev. Lett.* **103**, 120502 (2009). doi:10.1103/PhysRevLett.103.120502 Medline

12. R. Islam *et al*., Onset of a quantum phase transition with a trapped ion quantum simulator. *Nat. Commun.* **2**, 377 (2011). doi:10.1038/ncomms1374 Medline

13. J. W. Britton *et al*., Engineered two-dimensional Ising interactions in a trapped-ion quantum simulator with hundreds of spins. *Nature* **484**, 489 (2012). doi:10.1038/nature10981 Medline

14. A. Khromova *et al*., Designer spin pseudomolecule implemented with trapped ions in a magnetic gradient. *Phys. Rev. Lett.* **108**, 220502 (2012). doi:10.1103/PhysRevLett.108.220502 Medline

15. K. Kim *et al*., Quantum simulation of frustrated Ising spins with trapped ions. *Nature* **465**, 590 (2010). doi:10.1038/nature09071 Medline

16. E. E. Edwards *et al*., Quantum simulation and phase diagram of the transverse-field ising model with three atomic spins. *Phys. Rev. B* **82**, 060412 (2010). doi:10.1103/PhysRevB.82.060412

17. S. Olmschenk *et al*., Manipulation and detection of a trapped Yb^+ hyperfine qubit. *Phys. Rev. A* **76**, 052314 (2007). doi:10.1103/PhysRevA.76.052314

18. See supplementary materials on *Science* Online.

19. K. Binder, Critical properties from Monte Carlo coarse graining and renormalization. *Phys. Rev. Lett.* **47**, 693 (1981). doi:10.1103/PhysRevLett.47.693

20. C. Shen, L.-M. Duan, Correcting detection errors in quantum state engineering through data processing. *New J. Phys.* **14**, 053053 (2012). doi:10.1088/1367-2630/14/5/053053

21. W. C. Campbell *et al*., Ultrafast gates for single atomic qubits. *Phys. Rev. Lett.* **105**, 090502 (2010). doi:10.1103/PhysRevLett.105.090502 Medline

22. C.-C. J. Wang, J. K. Freericks, Intrinsic phonon effects on analog quantum simulators with ultracold trapped ions. *Phys. Rev. A* **86**, 032329 (2012). doi:10.1103/PhysRevA.86.032329

23. R. Moessner, S. L. Sondhi, Ising models of quantum frustration. *Phys. Rev. B* **63**, 224401 (2001). doi:10.1103/PhysRevB.63.224401

24. A. W. Sandvik, Ground states of a frustrated quantum spin chain with long-range interactions. *Phys. Rev. Lett.* **104**, 137204 (2010). doi:10.1103/PhysRevLett.104.137204 Medline

25. Quantum Monte Carlo algorithms can be used to calculate static equilibrium properties of the transverse field Ising model for large numbers of interacting spins, so ground states and static correlation functions can indeed be calculated for large systems (*23*). However, the calculation of dynamics and nonequilibrium behavior of quantum spin models is not currently feasible for these Monte Carlo approaches, and in the presence of frustrated long-range interactions, the general behavior of such systems requires exact diagonalization. Other techniques such as the density matrix renormalization group become too difficult with long-range interactions. Because the size of the Hilbert space grows exponentially with the number of spins, sparse-matrix techniques such as the Lanczos method must therefore be used. Current state-of-the-art work on such systems is limited to sizes on the order of 30 to 35 spins (*24*).

26. S.-L. Zhu, C. Monroe, L.-M. Duan, Trapped ion quantum computation with transverse phonon modes. *Phys. Rev. Lett.* **97**, 050505 (2006). doi:10.1103/PhysRevLett.97.050505 Medline

27. D. Leibfried, R. Blatt, C. Monroe, D. Wineland, Quantum dynamics of single trapped ions. *Rev. Mod. Phys.* **75**, 281 (2003). doi:10.1103/RevModPhys.75.281

28. M. Acton *et al*., Near-perfect simultaneous measurement of a qubit register. *Quant. Inf. Comp.* **6**, 465 (2006).